Direct observation of highly anisotropic electronic and optical nature in indium telluride

Geoffroy Kremer, Aymen Mahmoudi, Meryem Bouaziz, Cléophanie Brochard-Richard, Lama Khalil, Debora Pierucci, François Bertran, Patrick Le Fèvre, Mathieu G Silly, Julien Chaste, et al.

Direct observation of highly anisotropic electronic and optical nature in indium telluride

Geoffroy Kremer,[1,2] Aymen Mahmoudi,[1] Meryem Bouaziz,[1] Cléophanie Brochard-Richard,[1] Lama Khalil,[1] Debora Pierucci,[1] François Bertran,[3] Patrick Le Fèvre,[3] Mathieu G. Silly,[3] Julien Chaste,[1] Fabrice Oehler,[1] Marco Pala,[1] Federico Bisti,[4] and Abdelkarim Ouerghi[1,*]

[1]*Université Paris-Saclay, CNRS, Centre de Nanosciences et de Nanotechnologies, 91120 Palaiseau, Paris, France*
[2]*Institut Jean Lamour, UMR 7198, CNRS-Université de Lorraine, Campus ARTEM, 2 allée André Guinier, BP 50840, 54011 Nancy, France*
[3]*Synchrotron SOLEIL, L'Orme des Merisiers, Départementale 128, 91190 Saint-Aubin, France*
[4]*Dipartimento di Scienze Fisiche e Chimiche, Università dell'Aquila, Via Vetoio, 67100 L'Aquila, Italy*

(Received 15 March 2023; revised 4 June 2023; accepted 14 June 2023; published 11 July 2023)

Metal monochalcogenides (MX, M = Ga, In; X = S, Se, Te) offer a large variety of electronic properties depending on chemical composition, number of layers, and stacking order. InTe material has a one-dimensional chain structure, from which intriguing properties arise. Precise experimental determination of the electronic structure of InTe is needed for a better understanding of potential properties and device applications. In this study, by combining angle-resolved photoemission spectroscopy and density functional theory calculations, we demonstrate the stability of InTe in the tetragonal crystal structure, with a semiconducting character and an intrinsic p-type doping. The valence band maximum results in being located at the high symmetric M point with a high elliptical valley, manifesting a large effective mass close to the Fermi level. The longitudinal and transverse effective masses of the M valley are measured as 0.2 m_0 and 2 m_0, respectively. More specifically, we observe that the effective mass of the hole carriers is about ten times larger along the chain direction compared to the perpendicular one. Remarkably, the in-plane anisotropy of effective mass from the experiment and in theoretical calculations are in good agreement. These observations indicate a highly anisotropic character of the electronic band structure, making InTe of interest for electronic and thermoelectric applications.

DOI: 10.1103/PhysRevMaterials.7.074601

I. INTRODUCTION

Low dimensional electronic states bear fascinating emergent physics [1,2]. Recently, the electronic properties of two-dimensional (2D) materials [3], van der Waals (vdW) heterostructures [4], quantum well states confined on the surface/interfaces of semiconductors [5] or oxides [6], and topological surface states of strong topological insulators [7] have been investigated. The low dimension confinement is fascinating because, as what can happen in 1D systems for example, fundamentally important phenomena may emerge, such as the Peierls phase transition [8,9] or topological edge states [10].

In the case of the 2D materials, the anisotropic electronic band structure is typically a consequence of anisotropic crystal structure [11], because in the long-wavelength limit, short-range discreteness of the lattice is averaged out. Such lattice anisotropy can lead to highly anisotropic physical properties such as electric conductivity and phonon group velocity. Meanwhile, anisotropies in physical properties may also lead to device applications which are excessively difficult to obtain using isotropic materials. Among them, anisotropic 2D materials is one kind of system that possess different properties along different directions caused by the intrinsic anisotropic atoms' arrangement, mainly including black phosphorus [12], low-symmetry transition metal dichalcogenides [13–16], and group IV monochalcogenides [17–20]. Recently, a series of devices has been fabricated based on these anisotropic 2D materials [21]. One of the most pertinent examples in this context is the above mentioned black phosphorus [22,23], a 2D material with a highly anisotropic character and associated signatures in its in-plane thermal, electrical, and thermoelectric transport properties [12,24].

Recently, group-III monochalcogenides have attracted great attention due to their electronical, optical, and thermal properties [25,26]. Their crystal structure consists in covalently bound sheets, stacked vertically through vdW interactions, and with thickness dependent electronic properties [27,28]. In particular, they exhibit band gaps in the 1–3-eV range when the thickness is reduced to a few layers [29], corresponding to the visible light range, showing also high photoresponsivity [30]. Indium selenide (InSe) has first drawn considerable attention due to its high electron mobility and exists in a layered hexagonal structure, with potential application in photodetection and high-density storage [31]. The case of indium telluride (InTe) stands out in its chalcogenide family with a tetragonal crystal structure, mixing weak interactions and covalent bonds in a strongly anisotropic unit cell [32–35]. A recent work has been carried out on the exploration of the electronic properties of InTe hexagonal ultrathin films [36]. It has shown interesting results about the thickness dependence of the band gap in this compound, but in the case of anisotropic tetragonal InTe, the band structure is still not precisely understood and the consequences of unit cell anisotropy on the electronic properties have not been experimentally investigated.

*Corresponding author: abdelkarim.ouerghi@c2n.upsaclay.fr

In this work, we report the electronic properties of tetragonal InTe, where significant in-plane anisotropies are discovered. Using angle-resolved photoemission spectroscopy (ARPES), we map the band structure dispersion bringing out a highly anisotropic behavior of carriers. We determine the effective masses from the energy and momentum dispersion relationship at the valence band (VB) extrema. We find a high anisotropy reaching one order of magnitude between the effective masses depending on the crystal orientation. Such result is further supported by the excellent agreement of the density functional theory (DFT) calculated band structure with the experimental data. Complementary micro-Raman spectroscopy analysis is performed to better understand the structural properties of the crystal, namely by exploring the vibration frequencies of phonons corresponding to the characteristic vibrational modes of InTe. All data confirm the existence of relatively flat VB close to the Fermi level with rather large anisotropic effective masses. This leads to a large density of state (DOS) close to the Fermi level, that we propose to interpret as the origin of the peculiar thermoelectric properties of the material, in relation with its high Seebeck coefficient [34].

II. METHODS

The Raman spectroscopy measurements were performed on a Horiba Scientific LabRAM HR at an excitation of $\lambda = 532$ nm, in a backscattering geometry in parallel-polarized configuration, with a 360° rotational sample stage. The spectral resolution is $\sim 0.7\,\mathrm{cm}^{-1}$ for the grating of 1800 grooves per mm. The spectrometer was calibrated with a pristine silicon sample. ARPES experiments were performed at the CASSIOPEE beamline of the SOLEIL synchrotron light source. The CASSIOPEE beamline is equipped with a Scienta R4000 hemispherical electron analyzer whose angular acceptance is ±15° (Scienta wide angle lens). Commercial InTe samples from the 2D Semiconductors company were cleaved in UHV at a base pressure better than 1×10^{-10} mbar. The experiment was performed at $T = 50$ K and at 80 eV photon energy if not explicitly specified. The total angle and energy resolutions were 0.25° and 16 meV, respectively. The incident photon beam was focused into a 50-μm spot (in diameter) on the sample surface. All ARPES measurements were performed with a linear horizontal polarization. Core level photoemission spectroscopy was performed at the TEMPO beamline of the Synchrotron SOLEIL. The TEMPO beamline is equipped with a MB scientific A-1 photoelectron analyzer. The measurements were done at room temperature in a base pressure of 3×10^{-10} mbar. The spot size of the incident photon beam was of 300 μm full width at half maximum on the sample surface. For the curve fitting procedure, a Shirley background was subtracted to account for the secondary electron background, and core level peaks were approximated using the Voight function.

III. RESULTS AND DISCUSSION

Indium telluride crystallizes in a TlSe-type structure [33], best described by tetragonal space group $I4/mcm$ with cell parameters at 300 K, $a = b = 8.62$ A, and $c = 7.22$ A. It can be decomposed as $In^{1+}In^{3+}Te_2^{2-}$, which highlights the two inequivalent types of In atom in the unit cell. While Te atoms occupy a single type of crystallographic site (Wyckoff position 8*h*), In atoms are distributed over two distinct crystallographic sites, named hereafter In^{3+} and In^{1+}, respectively [Fig. 1(a)]. The In^{3+} ions are coordinated to the Te^{2-} ions, forming covalently bound tetrahedra, arranged in infinite chains along the *c* axis. The remaining In^{1+} ions are placed regularly between the $(InTe_2)^-$ polyhedra and weakly bound to the Te atoms. These In^{1+} ions are known to display large anisotropic thermal displacement parameters [32]. Due to the weak interactions between $(InTe_2)^-$ chains, the crystal tends to cleave along the (110) planes, along the plane of weakly bound In^{1+} ions [34] [Fig. 1(b)].

All InTe single crystals were purchased from 2D Semiconductors (USA). The single-crystalline nature was confirmed by ARPES [37], which further evidences that the natural cleavage plane corresponds to the (110) plane (see discussion below). Micro-Raman and x-ray photoemission spectroscopy (XPS) measurements confirm the expected stoichiometry of In and Te in the crystal. A typical room temperature micro-Raman spectrum is shown in Fig. 1(c) (black line). The E_g and A_{1g} peaks are observed at frequencies in agreement with those previously reported [33,38]: the E_g peak at 48 and 139 cm^{-1} and the A_{1g} peak at 127 cm^{-1}. For the A_{1g} mode, only Te atoms move in the *xy* plane, whereas for the E_g mode, In^{3+} and Te atoms vibrate along the *xy* plane and *z* direction, respectively. In both modes, the In^{1+} atoms do not exhibit any displacement. Additional peaks are found in low frequency at 46 cm^{-1} which can be attributed to multiple unit cell shearing and breathing modes. The emergence of these low frequency phonon modes indicates that the good crystal quality and the overall Raman response is consistent with expected $I4/mcm$ symmetry [33]. We have then studied the anisotropy of InTe in detail by polarization-dependent Raman spectroscopy at $\lambda = 532$ nm laser excitation (room temperature). The intensity of Raman modes depends on the linear polarization angle of incident light (θ) in a backscattering Raman configuration. As shown in Fig. 1(d), where the polar plot of the A_{1g} Raman line intensity against the in-plane angle θ is shown, the A_{1g} (127 cm^{-1}) Raman mode has the largest intensity when the light polarization is aligned along the *c* axis (90°/270°) and reaches a minimum value for the perpendicular direction [1–10] (0°/180°). This behavior is attributed to the in-plane high optical anisotropy properties of the (110) InTe surface.

The strong asymmetry of the crystalline structure of InTe along the *a* and *c* axes is also present in the (110) cleavage plane [see Fig. 1(b)], and it is expected to also appear in the electronic properties of the material. To uncover this, we have studied the electronic anisotropy of the VB as a function of angle by ARPES combined with DFT calculations [37]. Additional high-resolution photoemission spectra for In 4*d*, and Te 4*d* are recorded using a photon energy of 80 eV (Fig. S1 in the Supplemental Material [39]). The experimental data points are displayed in dots and the red solid lines represent the envelope of the fitted components [40]. The In 4*d* spectrum presents two peaks at a binding energy (BE) of 17.7 and 18.6 eV, which can be attributed to the In $4d_{5/2}$ and In $4d_{3/2}$ [spin-orbit (SO) splitting of 0.9 eV] [Fig. S1(a)]. Similarly, two components

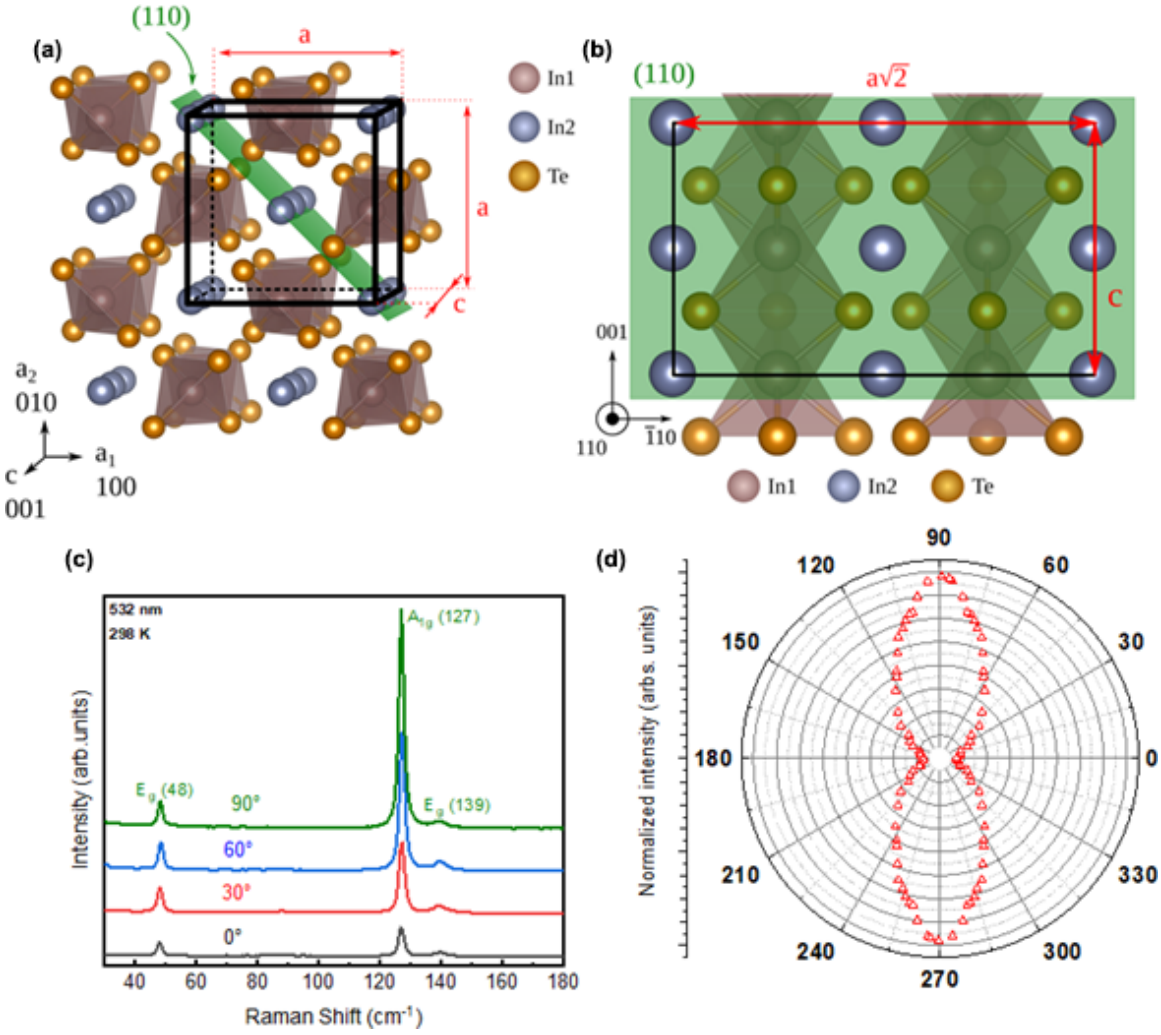

FIG. 1. Crystal structure and structural properties of InTe: (a) Crystal structure of $I4/mcm$ tetragonal InTe crystal, showing to two inequivalent In atoms (In^{1+} blue color, In^{3+} brown) and the preferential (110) cleavage plane (green color). (b) Local atomic arrangement of the (110) plane, displaying a strong structural anisotropy between the two in-plane directions, with infinite covalently-bounded chains along the c axis and weak interaction along [1–10]. (c) Polar-plot dependent Raman spectra of InTe with different in-plane orientation angle theta. For the A_{1g} mode, only Te atoms move in the xy plane, whereas for the E_g mode, In^{3+} and Te atoms vibrate along the xy plane and z direction, respectively. In both modes, the In^{1+} atoms do not exhibit any displacement. (d) Polar plot of the A_{1g} Raman line intensity against the in-plane angle theta. $\Theta = 0$ and 90° indicate the a- and c-axis direction, respectively.

are also present for the Te 4d peak, corresponding to the Te $4d_{5/2}$ BE = 40.3 eV and $4d_{3/2}$ BE = 41.8 eV with a SO splitting of 1.5 eV [Fig. S1(b)]. No other components are detected in the spectra, including oxygen, which demonstrates the absence of surface oxidation in the probed area. Moreover, a quantitative analysis, obtained using the intensity of the In 4d and Te 4d peaks, shows a In:Te ratio of about 1, confirming the monochalcogenide stoichiometry of the InTe crystal.

Electronic band structure features, such as dimensionality of the band structure and locations of their conduction band minima (CBM) and valence band maxima (VBM), provide important insight into the understanding of chalcogenide materials such as InTe. Before discussing the electronic band structure measurements, it is of interest to describe the first Brillouin zone (BZ) of InTe as shown in Fig. 2(a). With a tetragonal body-centered crystal structure ($I4/mcm$) associated to inequivalent unit cell parameters a and c, with $c < a$, the BZ is an elongated dodecahedron, referred as BCT_1 [41]. Due to the body-centered crystal structure in real space, the closest vectors of the reciprocal space are of type 110, 011, and 101, akin to body-centered cubic materials. Note that we maintain the use of a nonprimitive tetragonal unit cell in the real and reciprocal space. This choice is motivated by the colinearity between the corresponding real and reciprocal basis in the nonprimitive tetragonal form, while it is lost when using the smaller (and less symmetric) primitive cell. In this notation, the high-symmetry X point lies at $\frac{1}{2}$ (1, 1, 0) in reciprocal space and the ΓX direction simply aligns with the [1, 1, 0] real space vector. Similarly, the M, Z, and P coordinates are (1,0,0), (0,0,1), $\frac{1}{2}$ (1, 1, 1) in reciprocal space, so that ΓM, ΓZ, and ΓP align with [1, 0, 0], [0, 0, 1] and [1, 1, 1] in real space, respectively. From Fig. 2(a), we see that the BCT_1 BZ is elongated along ΓZ with the existence of the Z_1MZ_1 segment along the ΓZ direction in the MXP

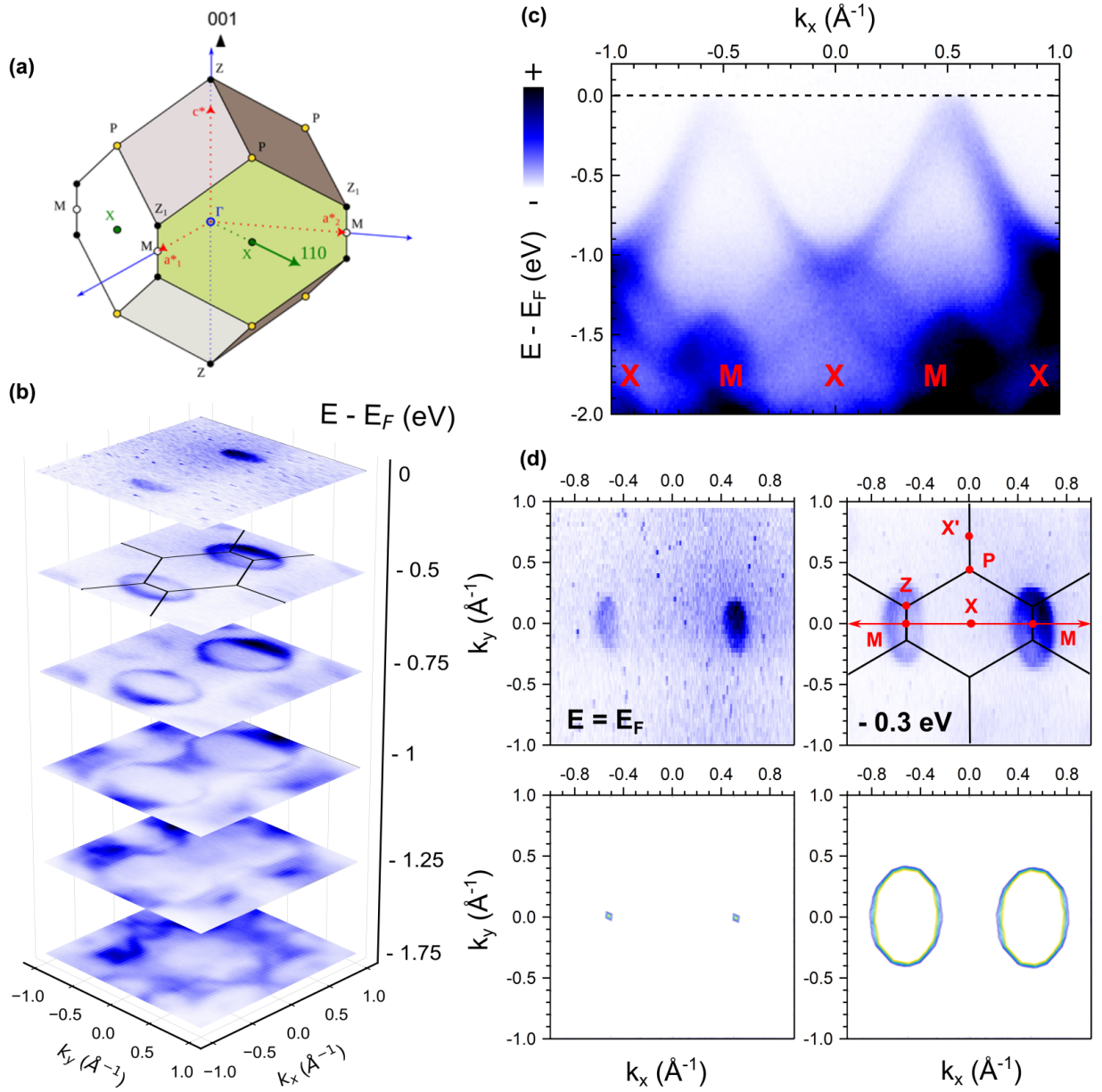

FIG. 2. Electronic band structure of InTe: (a) Brillouin zone of the body-centered-tetragonal unit cell of InTe. The high-symmetry points are indicated; (b) ARPES 3D mapping in the *MXP* plane; (c) ARPES map of InTe along the *MXM* direction. (d) Comparison of experimental and DFT isoenergic ARPES maps of InTe at E_F and -0.3 eV.

face (green color), which is the direct consequence of the shorter c axis in real space ($c < a$). The shape of the BZ is particularly relevant to the experimental ARPES parameters, as we want to sample a fraction of momentum space, large enough to hold the signature of the expected anisotropy and to support quantitative analysis with theoretical DFT result.

We now focus our attention on the experimental determination of the in-plane ARPES data (k_x, k_y) acquired along the cleaved (110) plane. We particularly focus on the $\overline{XMP}$ plane [green color Fig. 2(a)], in which normal is [110] in reciprocal space and also [110] in real space (using the nonprimitive orthogonal cell in both spaces). The $\overline{XMP}$ is particularly relevant as it should hold the signature of the anisotropy of the unit cell along MZ_1 (i.e., parallel to ΓZ reciprocal space, c-axis real space).

In Fig. 2(b), we show the acquired experimental ARPES data by plotting a series of isoenergetic cuts along the $\overline{XMP}$ plane. We confirm that electronic states in the vicinity of the Fermi level are only found around the M points. Moreover, the ARPES measurement shows a single set of two equivalents M points, which indicates that our InTe sample is fully monocrystalline. In Fig. 2(c), we report the InTe band structure projection on the surface BZ along the $\overline{MXM}$ high-symmetry direction using a photon energy of 80 eV (see the k_z dispersion in Fig. 3). It shows that the VB is characterized by a downward dispersion in the vicinity of the M points. Figure 2(d) further evidences the strong in-plane anisotropy of

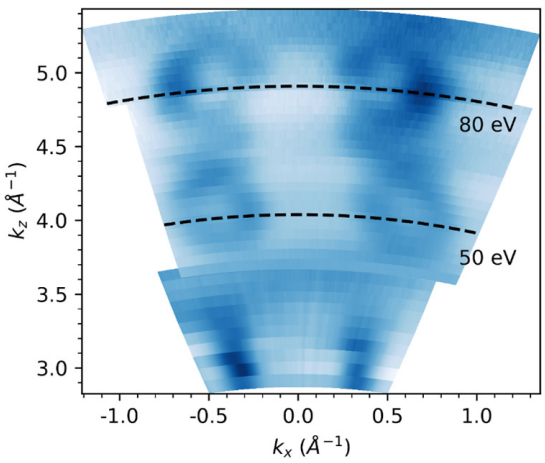

FIG. 3. Photon energy dependent ARPES measurements converted to $I(k_z, k_x)$ ARPES map ($E-E_F = -0.5$ eV) for InTe single crystal. The two dashed lines highlight the photon energies corresponding to the *M*-*X*-*M* high-symmetry direction.

the effective hole mass for InTe by showing the elliptical-like shape of the Fermi surface at the M point. The comparison between experimental measurements and DFT calculations of the isoenergetic contours in the $\overline{MXP}$ plane [bottom panel in Fig. 2(d)] confirms the presence of states only around the $\bar{M}$ point in the vicinity of the Fermi level. This is in good agreement with our experimental data and further confirms the natural (110) cleavage plane of InTe [Fig. 1(b)], which sets the experimental axis of our ARPES data, with the $\overline{XMP}$ plane being sampled in-plane along (k_x, k_y) and k_y aligning with ΓZ and the c axis of the tetragonal unit cell.

In order to gain more insight on the electronic structure of InTe, we performed electronic band structure calculations using both Perdew-Burke-Ernzerhof (PBE) [42] and Heyd-Scuseria-Ernzerhof (HSE) hybrid functionals [43]. Figure 4(a) shows the measured band structure in the vicinity of the $\overline{MXM}$ direction at large scale. The top of the VB at the M point is mostly formed by p orbitals of Te and s orbitals of In, respectively, while the conduction band (CB) is mostly composed by s orbitals of Te and p orbitals of In, as can be seen from the orbital projected LDOS plotted in Figs. S2 and S3 [39]. The electronic structure from the Fermi level down to 3 eV binding energy (BE) is in good agreement with our electronic structure calculations [Figs. 4(b) and 4(c)], although the energy separation between the top of the VB at M and X is slightly underestimated with PBE [Fig. 4(b)]. Specifically, we demonstrate the agreement between the ARPES results and DFT calculations. In both theory and experiments the VB maximum at the M point is located at lower BE than at the X point. The energy separation between the M and X is comparable: 1 eV in experimental data [Fig. 4(b)], 1 eV in PBE, and 1.1 eV in HeydScuseriaErnzerhof (HSE) [Figure 4(c)]. Finally, it is worthwhile to mention that a local CBM is also situated at the M point for both the PBE and HSE functionals. However, the energy separation at this high-symmetry point is substantially underestimated in PBE. The value obtained with the hybrid functional is more accurate and is expected to underestimate the quasiparticle band gap by no more than 10%, as observed in other members of the indium monochalcogen and MX_2 family [44].

In order to evaluate the strong in-plane anisotropy of the VB dispersion near the M point, we perform an analysis of the curvature of the VBs from the ARPES measurements in two separate directions. We present in Figs. 5(b) and 5(c) the electronic band structure along the two perpendicular directions of InTe around the M point. A parabolic fit is employed to describe the local curvature of the VB maximum at M, but it should be remarked that the curves present a significant non-parabolic character, leading to a degree of incertitude in the extracted value of the effective mass. The adopted quadratic function is indicated by a red-colored line in Figs. 5(b) and 5(c). We have determined the effective mass of the hole close to the M point of the BZ along the XMX and ZMZ high-symmetry directions. The experimental dispersion has been fitted with a parabolic model $E(k) = E + \hbar k^2/2m^*$ where m^* is the effective electron mass and $\hbar$ is the reduced Planck. We thus derive two experimental values of 0.2 m_0 and 2 m_0 (where m_0 is the free electron mass) at the M point along MX and MZ

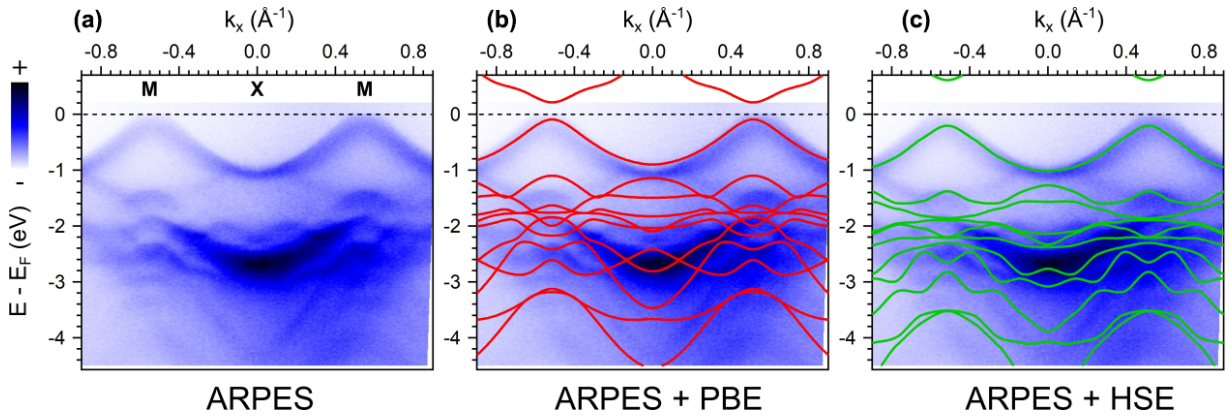

FIG. 4. ARPES data of InTe measured in the vicinity of the $\bar{M}$-$\bar{X}$-$\bar{M}$ high-symmetry direction compared with theoretical electronic band structure: (a) ARPES map of InTe along the MXM high-symmetry directions ($T = 50$ K and hv = 55 eV). (b),(c) Comparison between ARPES map and DFT calculations (PBE and HSE, respectively). The calculation was performed by considering an offset of 10% with respect to the MXM high-symmetry direction. For this photon energy, VBM is located at the M point.

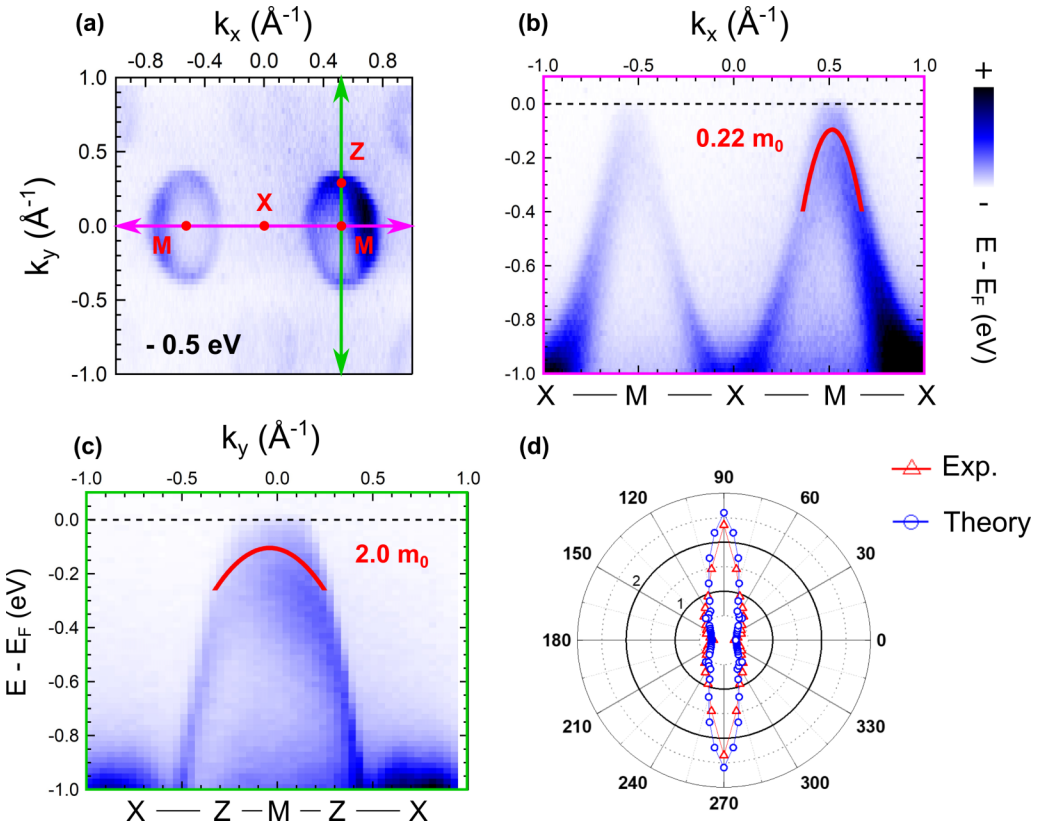

FIG. 5. Anisotropic effective hole masses of InTe near the valence band maximum: (a) Isoenergic ARPES maps of InTe at −0.5 eV below E_F. ARPES cut data along the in-plane momentum defined by the angle θ [see colored lines in Fig. 4(a) for definition] for InTe. All the data sets are centered around the M point at which VBM is located; (b),(c) ARPES cuts along and perpendicular to the MXM direction. The red lines indicate a quadratic function fitting the dispersions of the top-most bands. (d) Comparison of experimental and DFT polar plot of the effective mass against the in-plane angle theta. Theta = 0 and 90° indicates the a- and c-axis direction, respectively.

(MZ_1), respectively. These values agree very well with the PBE and HSE calculations, suggesting that many body effects are not important close to the top of the VB at M. One can notice that this mass is close to m_0 which implies that the InTe band is poorly dispersive. This feature leads to the appearance of a large DOS near the top of the VB of InTe, as observed by DFT calculations. The emergence of the high DOS can enhance thermoelectric transport properties such as the same phenomena observed in the Si doped InSe [45].

The in-plane anisotropic character of VB dispersion is analyzed in more detail in Fig. 5(d). There we plot in polar coordinates the value of the relative effective mass m/m_0 computed from the parabolic fit of the ARPES data (red triangle) and DFT (blue circle) against the in-plane angle theta, with $\theta = 90$ along the ΓZ direction (real space c axis) and $\theta = 0$ along the MXM high-symmetry direction. Note that the θ angle, defined here in reciprocal space, is equivalent to the polar coordinate used for the anisotropic Raman analysis in real space [Fig. 1(d)]. The plot clearly shows a twofold symmetry and the strong in-plane anisotropy of the effective hole mass for InTe. We retrieve the specific values obtained previously for the high-symmetry lines at $\theta = 0/180°$ [MX] and $\theta = 90/270°$ [MZ], respectively. Due to the nonparabolic dispersion of the VB, our experimental determination of the effective mass is sensitive to the fitting range. Here, the (one dimensional) fitting range is fixed to 1/8 of the M-X length in reciprocal space. If this fitting range is doubled, the experimental effective masses may change up to 10%. Comparing our experimental effective mass to first principles calculations, we obtain an overall good agreement, with 2 m_0 along the infinite $(InTe2)^-$ chains (c axis, ΓZ direction) and 0.2 m_0 perpendicular to it. As electron-electron and electron-phonon interactions, as well as atomic spin-orbit coupling of InTe, are not considered in our DFT calculations, local discrepancies can exist between the experimental and theoretical band structures and effectives masses.

In summary, we have presented an exhaustive study of the electronic band structure of InTe cleaved along the (110) surface, combining spectroscopic tools and theoretical investigations. Using polarization-dependent Raman spectroscopy and ARPES, we characterized the anisotropic character of tetragonal InTe and we relate each parameter to the crystal structure and local orientation. We have found that InTe is stable in the tetragonal phase and is a 0.4 eV band gap semiconductor with high p doping. We systematically investigated in-plane directional dependence of the effective hole masse of the VB of InTe in the vicinity of the Fermi level. The hole effective mass of the M valley exhibits a strong anisotropy, about ten times heavier along the $(InTe2)^-$ chains, c axis, than along the direction perpendicular to it. The in-plane

anisotropy of the hole effective masses in InTe is larger than that in black phosphorus which also shows anisotropic optical and electronic properties. In this context, InTe can be considered a highly anisotropic material in terms of the low energy hole carrier dynamics, which makes this material a promising thermoelectric candidate for highly anisotropic semiconducting electronics. The highly anisotropic character of the hole carriers as well as possibility of the electron-electron and electron-phonon interactions may lead to collective electron order such as charge density waves, which has already been observed for doped samples and that could be explored with ARPES in the future.

The data sets generated during and/or analyzed during the current study are available from the corresponding author on reasonable request.

ACKNOWLEDGMENTS

We acknowledge the financial support by MagicValley (Grant No. ANR-18-CE24-0007), Graskop (Grant No. ANR-19-CE09-0026), 2D-on-Demand (Grant No. ANR-20-CE09-0026), and MixDferro (Grant No. ANR-21-CE09-0029), as well as the French technological network RENATECH.

The authors declare no competing interests.

[1] M. Naamneh, E. B. Guedes, A. Prakash, H. M. Cardoso, M. Shi, N. C. Plumb, W. H. Brito, B. Jalan, and M. Radović, Low-dimensional electronic state at the surface of a transparent conductive oxide, Commun. Phys. **5**, 317 (2022).

[2] H. Li, W. H. Brito, E. B. Guedes, A. Chikina, R. T. Dahm, D. V. Christensen, F. M. Chiabrera S.Yun, N. C. Plumb, M. Shi *et al.*, Reconstruction of low dimensional electronic states by altering the chemical arrangement at the $SrTiO_3$ surface, Adv. Funct. Mater. **33**, 2210526 (2023).

[3] L. Li, G. J. Ye, V. Tran, R. Fei, G. Chen, H. Wang, J. Wang, K. Watanabe, T. Taniguchi, L. Yang *et al.*, Quantum oscillations in a two-dimensional electron gas in black phosphorus thin films, Nat. Nanotechnol. **10**, 608 (2015).

[4] K. S. Novoselov, A. Mishchenko, A. Carvalho, and A. H. Castro Neto, 2D materials and van der Waals heterostructures, Science **353**, aac9439 (2016).

[5] M. Hajlaoui, S. Ponzoni, M. Deppe, T. Henksmeier, D. J. As, D. Reuter, T. Zentgraf, G. Springholz, C. M. Schneider, S. Cramm, and M. Cinchetti, Extremely low-energy ARPES of quantum well states in cubic-GaN/AlN and GaAs/AlGaAs heterostructures, Sci. Rep. **11**, 19081 (2021).

[6] T. C. Rödel, F. Fortuna, S. Sengupta, E. Frantzeskakis, P. Le Fèvre, F. Bertran, B. Mercey, S. Matzen, G. Agnus, T. Maroutian *et al.*, Universal fabrication of 2D electron systems in functional oxides, Adv. Mater. **28**, 1976 (2016).

[7] C. Lin, M. Ochi, R. Noguchi, K. Kuroda, M. Sakoda, A. Nomura, M. Tsubota, P. Zhang, C. Bareille, K. Kurokawa *et al.*, Visualization of the strain-induced topological phase transition in a quasi-one-dimensional superconductor $TaSe_3$, Nat. Mater. **20**, 1093 (2021).

[8] J. R. Ahn, J. H. Byun, H. Koh, E. Rotenberg, S. D. Kevan, and H. W. Yeom, Mechanism of Gap Opening in a Triple-Band Peierls System: In Atomic Wires on Si, Phys. Rev. Lett. **93**, 106401 (2004).

[9] S. Cheon, T. H. Kim, S. H. Lee, and H. W. Yeom, Chiral solitons in a coupled double Peierls chain, Science **350**, 182 (2015).

[10] J. Zhang, Y. Lv, X. Feng, A. Liang, W. Xia, S. K. Mo, C. Chen, J. Xue, S. A. Yang, L. Yang *et al.*, Observation of dimension-crossover of a tunable 1D Dirac fermion in topological semimetal $NbSi_xTe_2$, npj Quantum Mater. **7**, 54 (2022).

[11] S. W. Jung, S. H. Ryu, W. J. Shin, Y. Sohn, M. Huh, R. J. Koch, C. Jozwiak, E. Rotenberg, A. Bostwick, and K. S. Kim, Black phosphorus as a bipolar pseudospin semiconductor, Nat. Mater. **19**, 277 (2020).

[12] Y. Xu, Z. Shi, X. Shi, K. Zhang, and H. Zhang, Recent progress in black phosphorus and black-phosphorus-analogue materials: Properties, synthesis and applications, Nanoscale **11**, 14491 (2019).

[13] L. S. Hart, J. L. Webb, S. Dale, S. J. Bending, M. Mucha-Kruczynski, D. Wolverson, C. Chen, J. Avila, and M. C. Asensio, Electronic bandstructure and van der Waals coupling of $ReSe_2$ revealed by high-resolution angle-resolved photoemission spectroscopy, Sci. Rep. **7**, 5145 (2017).

[14] B. S. Kim, W. S. Kyung, J. D. Denlinger, C. Kim, and S. R. Park, Strong one-dimensional characteristics of hole-carriers in ReS_2 and $ReSe_2$, Sci. Rep. **9**, 2730 (2019).

[15] D. Wolverson, S. Crampin, A. S. Kazemi, A. Ilie, and S. J. Bending, Raman spectra of monolayer, few-layer, and bulk $ReSe_2$: An anisotropic layered semiconductor, ACS Nano **8**, 11154 (2014).

[16] E. Lorchat, G. Froehlicher, and S. Berciaud, Splitting of interlayer shear modes and photon energy dependent anisotropic raman response in N-Layer $ReSe_2$ and ReS_2, ACS Nano **10**, 2752 (2016).

[17] Z. Wang, C. Fan, Z. Shen, C. Hua, Q. Hu, F. Sheng, Y. Lu, H. Fang, Z. Qiu, J. Lu *et al.*, Defects controlled hole doping and multivalley transport in SnSe single crystals, Nat. Commun. **9**, 47 (2018).

[18] I. Suzuki, Z. Lin, S. Kawanishi, K. Tanaka, Y. Nose, T. Omata, and S. I. Tanakad, Direct evaluation of hole effective mass of SnS–SnSe solid solutions with ARPES measurement, Phys. Chem. Chem. Phys. **24**, 634 (2022).

[19] Y. Yang, S. C. Liu, Y. Wang, M. Long, C. M. Dai, S. Chen, B. Zhang, Z. Sun, Z. Sun, C. Hu *et al.*, In-plane optical anisotropy of low-symmetry 2D GeSe, Adv. Opt. Mater. **7**, 1801311 (2019).

[20] P. Mishra, H. Lohani, A. K. Kundu, R. Patel, G. K. Solanki, K. S. R. Menon, and B. R. Sekhar, Electronic structure of germanium selenide investigated using ultra-violet photo-electron spectroscopy, Semicond. Sci. Technol. **30**, 075001 (2015).

[21] Z. Muhammad, Y. Li, G. Abbas, M. Usman, Z. Sun, Y. Zhang, Z. Lv, Y. Wang, and W. Zhao, Temperature modulating fermi level pinning in 2D GeSe for high-performance transistor, Adv. Electron. Mater. **8**, 2101112 (2022).

[22] J. Miao, L. Zhang, and C. Wang, Black phosphorus electronic and optoelectronic devices, 2D Mater. **6**, 032003 (2019).

[23] Y. Zhou, M. Zhang, Z. Guo, L. Miao, S. T. Han, Z. Wang, X. Zhang, H. Zhang, and Z. Peng, Recent advances in black

phosphorus-based photonics, electronics, sensors and energy devices, Mater. Horiz. **4**, 997 (2017).

[24] F. Xia, H. Wang, and Y. Jia, Rediscovering black phosphorus as an anisotropic layered material for optoelectronics and electronics, Nat. Commun. **5**, 4458 (2014).

[25] D. A. Bandurin, A. V. Tyurnina, G. L. Yu, A. Mishchenko, V. Zólyomi, S. V. Morozov, R. K. Kumar, R. V. Gorbachev, Z. R. Kudrynskyi, S. Pezzini *et al.*, High electron mobility, quantum Hall effect and anomalous optical response in atomically thin InSe, Nat. Nanotechnol. **12**, 223 (2016).

[26] Y. Lee, R. Pisoni, H. Overweg, M. Eich, P. Rickhaus, A. Patanè, Z. R. Kudrynskyi, Z. D. Kovalyuk, R. Gorbachev, K. Watanabe *et al.*, Magnetotransport and lateral confinement in an InSe van der Waals Heterostructure, 2D Mater. **5**, 035040 (2018).

[27] Z. Ben Aziza, D. Pierucci, H. Henck, M. G. Silly, C. David, M. Yoon, F. Sirotti, K. Xiao, M. Eddrief, J. C. Girard, and A. Ouerghi, Tunable quasiparticle band gap in few-layer GaSe/graphene van der Waals heterostructures, Phys. Rev. B **96**, 035407 (2017).

[28] T. Cao, Z. Li, and S. G. Louie, Tunable Magnetism and Half-Metallicity in Hole-Doped Monolayer GaSe, Phys. Rev. Lett. **114**, 236602 (2015).

[29] D. J. Terry, V. Zólyomi, M. Hamer, A. V. Tyurnina, D. G. Hopkinson, A. M. Rakowski, S. J. Magorrian, N. Clark, Y. M. Andreev, O. Kazakova *et al.*, Infrared-to-violet tunable optical activity in atomic films of GaSe, InSe, and their heterostructures, 2D Mater. **5**, 041009 (2018).

[30] X. Yuan, L. Tang, S. Liu, P. Wang, Z. Chen, C. Zhang, Y. Liu, W. Wang, Y. Zou, C. Liu *et al.*, Arrayed van der waals vertical heterostructures based on 2d gase grown by molecular beam epitaxy, Nano Lett. **15**, 3571 (2015).

[31] S. R. Tamalampudi, Y. Y. Lu, R. K. Upadhyay, R. Sankar, C. D. Liao, K. M. Boopathi, C. H. Cheng, F. C. Chou, and Y. T. Chen, High performance and bendable few-layered InSe photodetectors with broad spectral response, Nano Lett. **14**, 2800 (2014).

[32] J. Zhang, N. Roth, K. Tolborg, S. Takahashi, L. Song, M. Bondesgaard, E. Nishibori, and B. B. Iversen, Direct observation of one-dimensional disordered diffusion channel in a chain-like thermoelectric with ultralow thermal conductivity, Nat. Commun. **12**, 6709 (2021).

[33] S. Misra, C. Barreteau, J. C. Crivello, V. M. Giordano, J. P. Castellan, Y. Sidis, P. Levinský, J. Hejtmánek, B. Malaman, A. Dauscher *et al.*, Reduced phase space of heat-carrying acoustic phonons in single-crystalline InTe, Phys. Rev. Res. **2**, 043371 (2020).

[34] S. Misra, P. Levinský, A. Dauscher, G. Medjahdi, J. Hejtmánek, B. Malaman, G. J. Snyder, B. Lenoir, and C. Candolfi, Synthesis and physical properties of single-crystalline InTe: Towards high thermoelectric performance, J. Mater. Chem. C **9**, 5250 (2021).

[35] S. Misra, A. Léon, P. Levinský, J. Hejtmánek, B. Lenoir, and C. Candolfi, Enhanced thermoelectric performance of InTe through Pb doping, J. Mater. Chem. C **9**, 14490 (2021).

[36] A. V. Matetskiy, V. V. Mararov, A. N. Mihalyuk, N. V. Denisov, S. V. Eremeev, A. V. Zotov, and A. A. Saranin, Thickness-dependent electronic band structure in MBE-grown hexagonal InTe films, Phys. Rev. B **106**, 165301 (2022).

[37] H. Henck, D. Pierucci, J. Zribi, F. Bisti, E. Papalazarou, J.-C. Girard, J. Chaste, F. Bertran, P. Le Fèvre, F. Sirotti *et al.*, Evidence of direct electronic band gap in two-dimensional van der Waals indium selenide crystals, Phys. Rev. Mater. **3**, 034004 (2019).

[38] V. Rajaji, K. Pal, S. Ch. Sarma, B. Joseph, S. C. Peter, U. V. Waghmare, and C. Narayana, Pressure induced band inversion, electronic and structural phase transitions in InTe: A combined experimental and theoretical study, Phys. Rev. B **97**, 155158 (2018).

[39] See Supplemental Material at http://link.aps.org/supplemental/10.1103/PhysRevMaterials.7.074601 for high-resolution XPS measurements in Fig. S1 and additional DFT calculations in Figs. S2 and S3.

[40] L. Khalil, J. C. Girard, D. Pierucci, F. Bisti, J. Chaste, F. Oehler, C. Gréboval, U. Nguétchuissi Noumbé, J. F. Dayen, D. Logoteta *et al.*, Electronic band gap of van der Waals α-As2Te3 crystals, Appl. Phys. Lett. **119**, 043103 (2021).

[41] Moritz M. Hirschmann, Andreas Leonhardt, Berkay Kilic, Douglas H. Fabini, and Andreas P. Schnyder, Symmetry-enforced band crossings in tetragonal materials: Dirac and Weyl degeneracies on points, lines, and planes, Phys. Rev. Mater. **5**, 054202 (2021).

[42] J. P. Perdew, K. Burke, and M. Ernzerhof, Generalized Gradient Approximation Made Simple, Phys. Rev. Lett. **77**, 3865 (1996).

[43] A. V. Krukau, O. A. Vydrov, A. F. Izmaylov, and G. E. Scuseria, Influence of the exchange screening parameter on the performance of screened hybrid functionals, J. Chem. Phys. **125**, 224106 (2006).

[44] H. Henck, Z. Ben Aziza, D. Pierucci, F. Laourine, F. Reale, P. Palczynski, J. Chaste, M. G. Silly, F. Bertran, P. Le Fèvre *et al.*, Electronic band structure of two-dimensional WS_2/Graphene van der Waals heterostructures, Phys. Rev. B **97**, 155421 (2018).

[45] K. Hyoung Lee, M.-W. Oh, H.-S. Kim, W. H. Shin, K. Lee, J.-H. Lim, J.-I. Kim, and S.-I. Kim, Enhanced thermoelectric transport properties of n-type InSe due to the emergence of the flat band by Si doping, Inorg. Chem. Front. **6**, 1475 (2019).